Improving the Limit of Detection of Nanoscale Sensors by Directed Binding to High-Sensitivity Areas

Laurent Feuz,* Peter Jönsson, Magnus P. Jonsson, and Fredrik Höök*

Department of Applied Physics, Chalmers University of Technology, SE-41296 Gothenburg, Sweden

ARTICLE

ABSTRACT The revelation of protein—protein interactions is one of the main preoccupations in the field of proteomics. Nanoplasmonics has emerged as an attractive surface-based technique because of its ability to sense protein binding under physiological conditions in a label-free manner. Here, we use short-range ordered holes with a diameter of ~150 nm and a depth of ~50 nm as a nanoplasmonic template. A ~40 nm high cylindrical region of Au is exposed on the walls of the holes only, while the rest of the surface consists of TiO_2. Since the sensitivity is confined to the nanometric holes, the use of two different materials for the sensor substrate offers the opportunity to selectively bind proteins to the most sensitive Au regions on the sensor surface. This was realized by applying material-selective poly(ethylene glycol)-based surface chemistry, restricting NeutrAvidin binding to surface-immobilized biotin on the Au areas only. We show that under mass-transport limited conditions (low nM bulk concentrations), the initial time-resolved response of uptake could be increased by a factor of almost 20 compared with the case where proteins were allowed to bind on the entire sensor surface and stress the generic relevance of this concept for nanoscale sensors. In the scope of further optimizing the limit of detection (LOD) of the sensor structure, we present finite-element (FE) simulations to unravel spatially resolved binding rates. These revealed that the binding rates in the holes occur in a highly inhomogeneous manner with highest binding rates observed at the upper rim of the holes and the lowest rates observed at the bottom of the holes. By assuming a plasmonic field distribution with enhanced sensitivity at the Au—TiO_2 interface, the FE simulations reproduced the experimental findings qualitatively.

KEYWORDS: localized surface plasmon resonance (LSPR) · nanoplasmonics · label-free · biosensor · nanoholes · selective surface chemistry · poly(ethylene glycol) (PEG)

The human genome codes for about 20000 different types of proteins, and for a majority, the function is still unknown. Within the field of proteomics, significant efforts are therefore put into unraveling the function of proteins and in particular how they interact mutually and with other biological entities. Indeed, a major part of processes in biological pathways, such as cell signaling, enzymatic activity, and carrier-mediated transport, rely on various protein—ligand and protein—protein interactions. Common methods used to extract such information rely on chemical labeling of one or both of the interacting partners.[1] However, attachment of chemical labels adds significant preparative steps and, for complex biological systems, inhomogeneous labeling is often an issue of great concern. In certain cases, external labels may also alter the nature of the interactions. For these reasons, but also because of their potential to extract detailed information on interaction kinetics, label-free surface-sensitive methods, such as the quartz crystal microbalance (QCM),[2] electrical impedance (EI),[3] and surface plasmon resonance (SPR),[4] have increased in popularity. One key value of these methods stems from the fact that with one of two interacting partners bound on a sensor surface, binding reactions can be transduced to a detectable signal *via* changes in the mechanical, electrical, and/or optical properties of such devices. Hence, although surface immobilization may in this case influence the nature of the interaction, these techniques provide real-time recording of binding/unbinding reactions, which is often complicated when external labels are employed for detection. Recently, the conventional surface-based methods have met significant competition from miniaturized alternatives. The latter class of sensors offers the advantages of being compatible with large scale multiplexing using multiple sensor elements on the very same chip as well as the possibility of handling minute sample volumes by integrating microfluidics. The most popular ones are resonating or surface-stress sensitive cantilevers,[5,6] semiconducting nanowires,[7] and localized surface plasmon resonance (LSPR, or nanoplasmonic) systems,[8,9] each of which in principle are analogous to QCM, EI, and SPR, respectively.

A challenge for protein analytical tools in general and surface-based methods in particular is that different proteins,

*Address correspondence to laurent.feuz@chalmers.se, fredrik.hook@chalmers.se.

Received for review October 21, 2009 and accepted March 25, 2010.

Published online April 8, 2010.
10.1021/nn901457f

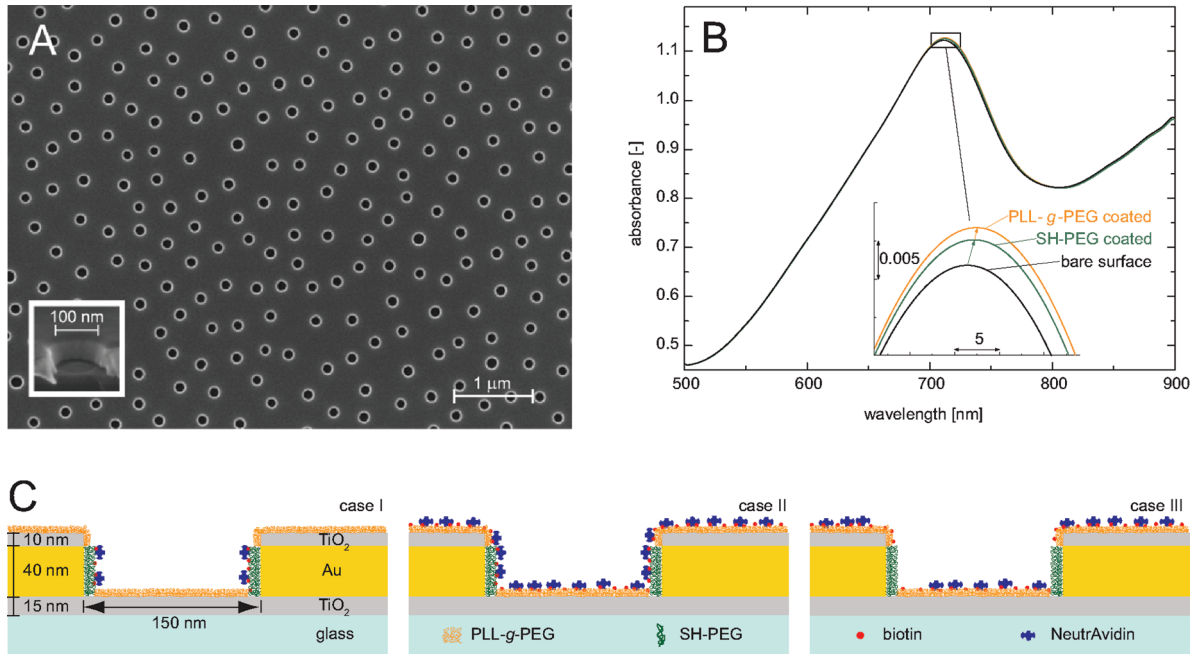

Figure 1. (A) Scanning electron microscopy (SEM) top-view image of the sensor, showing the short-range ordered nanoholes. The inset shows the cross-section of a hole imaged at 70° from the surface normal. (B) Extinction peak of the LSPR sensor immersed in buffer measured in transmission mode. The inset is a close-up of the peak and shows a representative sensor response (red-shift of the extinction peak) upon polymer adsorption. (C) Schematics of the cross-section of a hole and its characteristic dimensions, including adsorbed polymer layers (SH-PEG on Au and PLL-*g*-PEG on TiO_2) and NeutrAvidin. The latter either binds to biotin or is repelled by the PEG layer. In case I (left), only the SH-PEG on Au binds NeutrAvidin, in case II (middle) the whole surface of the sensor is rendered bioactive, while in case III (right) only the TiO_2 is biotinylated.

including various postmodified versions of the same, are present at concentrations that vary over several orders of magnitude.[10] Hence, in protein interaction studies, those present at high concentrations may mask low abundant (nM concentrations or lower) proteins. Consequently, in order to study the latter class, which is the main focus for examples in biomarker identification[11] and disease diagnostics,[12] two central requirements have to be met. First, the protein(s) of interest must interact selectively and specifically with the probe molecules on the sensor surfaces. This, in turn, means that the sensor surface has to be designed such that it is inert for all irrelevant proteins present in the sample, while the probe molecules must at the same time be immobilized such that they retain their native function. Second, since the measured surface coverage will essentially be proportional to the bulk concentration at low target concentrations, the transducer concept must be sensitive enough to detect low coverage of adsorbed proteins.

The first requirement can be approached by suitable surface chemistry. When grafted to surfaces at a sufficiently high density, poly(ethylene glycol) (PEG) is a very effective agent in preventing unspecific protein adsorption.[13] It bears the advantage that it can be coupled to a large palette of surface materials (metals, metal oxides, polymers) by having one of its ends carrying a specific chemical group (*e.g.*, thiols,[14] silanes,[15] mussel adhesive protein derivates,[16,17] polyelectrolytes,[18] or hydrophobic chains[19]) that mediates strong binding to the surface. Simultaneously, the other end of the PEG chain can either consist of an ordinary hydrophilic (hydroxy-, methoxy-) end group when protein repellence is desired, or a biofunctional moiety for specific target-molecule binding.[20,21] The proper combination of inert and bioactive PEGs on the very same surface provides an excellent platform for selective biosensing.[22−25]

The second requirement, detecting low abundant target molecules, is especially challenging for miniaturized nanoscale sensors, since the limit of detection (LOD) in terms of surface coverage, and hence bulk concentration, often becomes deteriorated when probing single or few nanoscale sensor elements. In addition, miniaturized sensors share one central feature, being the fact that the nanoscale sensitive regions generally exist in close proximity to significantly larger, insensitive regions. Hence, if the surrounding regions are not made inert, the majority of the interacting molecules will bind to regions outside the sensitive part of the sensor and thus be lost from a sensing point of view. However, as previously suggested from theoretical considerations,[26] the use of local surface chemistries controlling the binding of target molecules to occur on the sensitive regions only might turn this disadvantage into an advantage. Given that the sensitivity in terms of surface coverage is the same for nanoscale and macroscopic sensors, protein binding to locally functionalized regions may lead to sig-

nificantly increased local binding rates as compared with conventional techniques where molecules bind on the entire surface.

In the present work, this so far not explored opportunity is addressed both experimentally and theoretically using a specially designed nanoplasmonic sensor based on short-range ordered nanoholes in an optically thin gold film, partly mantled by TiO_2 as shown in Figure 1. The reason for choosing a Au−TiO_2-based nanoplasmonic sensor for this purpose is manifold. First, the measured nanoplasmonic response is directly proportional to the number of bound molecules, which makes detailed analysis of binding kinetics straightforward. Second, the plasmonic field of sensors based on short-range ordered nanoholes has previously been shown to be predominantly localized to the edges and void of such holes.[27] Third, the Au−TiO_2 system offers attractive possibilities in terms of material specific surface chemistries, while simultaneously providing the advantage of rendering an adhesion layer (typically Cr) between the two materials unnecessary. The presence of adhesion layers between Au and SiO_2 has previously been shown to lead to nonspecific target adsorption,[28] which in the context of detecting specific binding of low abundant proteins is a severe drawback. Yet, in the same study, the combination of thiol- and poly(L-lysine)-based PEG chemistry allowed for selective modification of Au−SiO_2 patterned surfaces. Since poly(L-lysine)-PEG can be used also on TiO_2 surfaces,[29] the combination of these two PEG systems is ideally suited for the present sensor. Fourth, by introducing a new fabrication method relying on scalable nanotechnology utilizing self-assembly of colloidal nanoparticles,[30] the top surface of the sensor could be coated with TiO_2. Thereby, the most sensitive surface area could be reduced to around 40 nm high gold rings inside the nanoholes. Having both a material and a surface area contrast between the most sensitive regions (Au; 12% of total surface area) and less sensitive regions (TiO_2; 88%) offers the opportunity to create small bioactive areas on the most sensitive regions only (see Figure 1).

The temporal variation in extinction peak position of the nanoplasmonic substrate was measured using a recently developed optical extinction spectroscopy setup enabling real-time monitoring of the peak position with a precision of $<5 \times 10^{-4}$ nm.[31] While providing a sensitivity in terms of LOD equal to or better than that of conventional SPR, transmission-mode readout is significantly simpler than conventional SPR readouts, which rely on prism or grating coupling of light.[32] Hence, combined with sensing performed from a small sample volume under stagnant (no flow) conditions, this offers one of the simplest possible solutions to surface-based sensing. Under these conditions, the rate of protein binding to the sensitive gold regions was compared with the situation when binding was allowed on the entire substrate or to the less sensitive TiO_2 regions only. The dependence of the temporally resolved response on target-concentration was evaluated using both finite element (FE) simulations, representing the spatially resolved binding rates for the different surface modifications, as well as a simplified analytical expression that aid an intuitive understanding of the benefit of the sensor design. The influence of an inhomogeneous field distribution around the nanoplasmonic active gold apertures is discussed in the context of the possibility to further develop the concept of localized target binding for improved sensor performance.

RESULTS AND DISCUSSION

TiO_2−Au-Based LSPR Sensor. The sensor was fabricated using a new approach combining colloidal lithography and dry-etching processes on a TiO_2(15 nm)−Au(40 nm)−TiO_2(15 nm)-coated glass slide. In brief, colloidal deposition on the TiO_2−Au−TiO_2 substrate was followed by evaporating a 40 nm Au mask. After colloidal removal, apertures were created by reactive ion etching and subsequent argon ion milling of Au, where the top Au layer acted as a sacrificial layer (see Materials and Methods for details). In this way, short-range ordered nanoplasmonic apertures with arbitrary depths could be fabricated. Figure 1A shows a scanning electron microscopy (SEM) image revealing apertures with a diameter of 154 ± 7 nm, a depth of about 50 nm, and an average center-to-center separation of 420 nm. The inset in panel A displays a cross-section of a single hole from a fractured sample. Both the top and cross-section images clearly display a strong material contrast between the top/bottom surfaces of the holes (dark material; TiO_2) and the walls of the holes (bright material; Au). Indeed, the clear visualization of the metal regions in the top-view images suggests slightly conical holes, which was taken into account in the FE simulations (see Materials and Methods and below for further details). Figure 1B shows the extinction spectrum of the structure in buffer with the maximum of the peak at around 720 nm. Using material specific surface chemistries, adsorption of biofunctionalized polymers on Au, followed by formation of a protein-repellent polymer layer on TiO_2, would potentially allow for low-abundant proteins to be directed and concentrated on the highly sensitive Au regions only. The material specific surface chemistry was realized by first exposing the substrate to thiol-modified PEG (SH-PEG), which binds to Au and does not adsorb on metal oxides.[33] This makes Au inert for poly(L-lysine)-*graft*-PEG (PLL-*g*-PEG),[18] which was used to subsequently coat TiO_2 by simply exposing the substrate to a solution containing PLL-*g*-PEG. Both types of PEGs were also available with biotin end groups, allowing the material of choice to be turned into a protein-binding region. Quartz crystal microbalance measurements were carried out to verify that the surface modification schemes performed as expected (data not shown). The inset in Figure 1B shows repre-

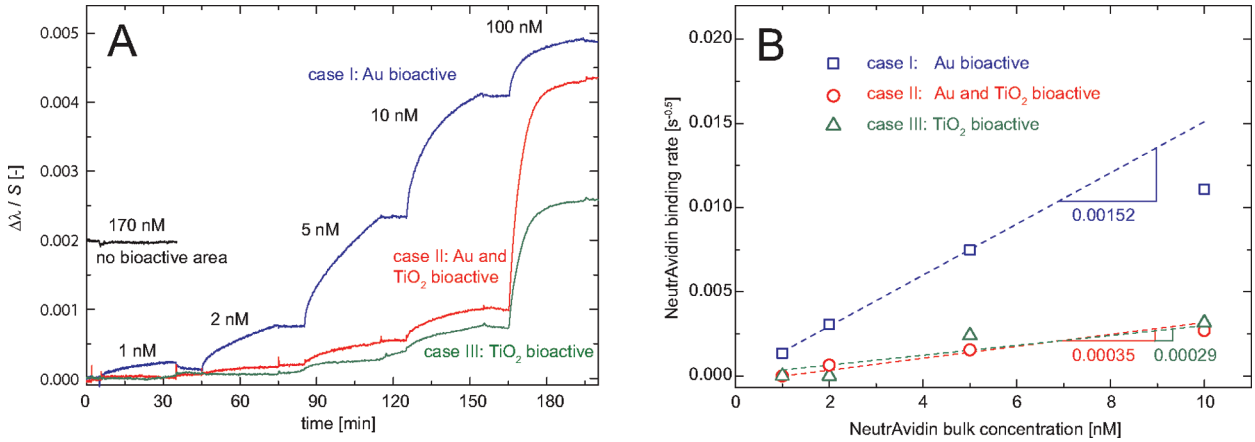

Figure 2. (A) Real-time monitoring of stepwise NeutrAvidin adsorption. Five NeutrAvidin solutions of increasing concentrations were injected subsequently to the sensor surface. The proteins were allowed to adsorb for 30 min at each concentration, followed by a 10 min buffer rinsing step. The peak shift was tracked using its centroid value.[31] The peak shift values Δλ have been normalized with the bulk sensitivity *S* of the individual sample. The curve in case III has been corrected for a constant drift of −0.0005 Δλ/*S* per hour (estimated from the slope of the curve when only buffer was present in the cell). The blue curve corresponds to case I (see Figure 1C left) where NeutrAvidin binds only to the Au region. The red curve represents case II where NeutrAvidin can bind on the entire sensor surface (see Figure 1C middle), and the green curve shows case III with NeutrAvidin binding on TiO_2 only (see Figure 1C right). The black curve shows the sensor response of a sample coated with PEGs containing no biotin. A NeutrAvidin solution (170 nM) was injected at *t* = 5 min. The curve has been offset by 0.002 for convenience. (B) NeutrAvidin binding rates for different protein bulk concentrations and surface functionalizations. The rates have been determined by extracting the initial slopes of the peak shift *versus* the square root of time curves and were normalized with the total sensor response upon saturation. The dashed lines are linear fits to the three points at the lowest concentrations for case I and to all the data points (including 100 nM, not shown) for case II and III. The slope values are listed for quantitative comparison.

sentative red-shifts of the plasmonic peak position upon adsorption of the polymer layers in buffer, corresponding to around 1 and 0.3 nm for adsorption of SH-PEG and PLL-*g*-PEG on the highly sensitive Au and slightly sensitive TiO_2 regions, respectively. The three different biofunctionalization schemes investigated are illustrated in Figure 1C: In case I (left), 20% of the SH-PEG chains carried a biotin end group that allows for selective binding of NeutrAvidin. In case II (middle), 20% of both the SH-PEG and the PLL-*g*-PEG were biotinylated, providing binding sites for NeutrAvidin on the whole surface, and in case III (right), only the PLL-*g*-PEG was biotinylated while pure SH-PEG was present on Au. The PEG chain density is believed to be somewhat higher on TiO_2 since the shorter PEG chains of the PLL-*g*-PEG (2 kDa) can pack more densely on the surface than the longer SH-PEG chains (3 kDa).[18,34] To promote exposure of the biotin end groups,[35] the biotinylated PEG chains were slightly longer than the pure PEG chains. The presence of biotin did not significantly influence the saturated peak shift (data not shown).

NeutrAvidin Binding from Low Concentration Solutions. Exposure of the sensors of case I (binding to Au only), case II (binding to both Au and TiO_2), and case III (binding to TiO_2 only) to low nM concentrations of NeutrAvidin solutions under stagnant conditions resulted in strikingly different responses (Figure 2A). In case I, where proteins are allowed to bind on Au only, NeutrAvidin concentrations of 1 nM resulted in a small but clearly detectable signal within seconds. In cases II and III, detectable signals are only obtained for ≥2 nM solutions, but with an 18 times slower response (see further below). In case I, about half of the saturated coverage is reached within 30 min after injection of a 5 nM solution, while in cases II and III, merely one-sixth of the saturated coverage is reached within this period of time. In fact, only one-third of the saturated coverage is reached after 30 min for a concentration of 10 nM in cases II and III. At higher concentrations (≥10 nM) for case I, the adsorption kinetics becomes markedly slowed down, suggesting a transition from mass-transport limited to reaction-controlled binding. This leads to a less pronounced sensor response, which is especially apparent for the 100 nM injection in case I. In cases II and III, a large initial response is observed only at 100 nM, resulting in saturated binding after 30 min, as verified from the fact that additional 100 nM injections did not induce further peak shifts (data not shown).

A qualitative explanation to the significantly faster response obtained in case I (binding to Au only) at low bulk concentrations (≤10 nM) is that proteins approaching the TiO_2 top-surface are repelled and can diffuse into adjacent biotin-modified Au regions. The result is a more rapid increase in NeutrAvidin coverage on the Au compared to case II, where proteins bind also to TiO_2. This interpretation is supported by the fact that the average distance between two holes is around 400 nm, and that the time for a molecule to diffuse such a distance is in the millisecond range. Hence, every molecule that gets close to the surface can potentially reach a hole within the time scale of the measurement.

As a negative control, a sample fully coated with PEG and thus without any bioactive area was exposed to a 170 nM NeutrAvidin solution. No detectable sensor re-

sponse was observed, verifying that the measured peak shifts in Figure 2A can be fully attributed to specific NeutrAvidin−biotin interactions. This also demonstrates the advantage of the TiO_2−Au based structure in comparison with work performed on SiO_2−Au based sensors. For the latter, exposure of a fully PEGylated surface to a 170 nM streptavidin solution led to a response in the order of 6% of the total signal recorded for a fully biotinylated surface.[28] This was attributed to unspecific adsorption of streptavidin to the less efficiently modified Cr adhesion layer between the SiO_2 and the Au. Since the adhesion layer used in most nanoplasmonic concepts coincides with the most sensitive area of the sensor, the improvement provided by the TiO_2−Au system is of general importance in the scope of analyzing specific interactions of low abundant proteins.

Quantification of Adsorption Kinetics. It should be noted that for all injection steps but the last one (100 nM), the attained coverage does not correspond to equilibrium conditions since the adsorption process has deliberately been terminated after 30 min by rinsing with buffer. For a quantitative analysis it is therefore not the coverage values after each step that should be compared but rather the initial rate of protein binding upon protein injection. In the diffusion limited regime, the protein surface concentration, c_s, scales with the square root of time:[36]

$$c_s(t) \propto c_0\sqrt{Dt} \qquad (1)$$

where c_0 is the NeutrAvidin concentration in the bulk solution, D is the diffusion coefficient of the protein, and t is time. The initial binding rates were determined by the slopes of linear fits to c_s *versus* $t^{1/2}$ plots (not shown) and are presented in Figure 2B for different protein bulk concentrations. With only Au bioactive (case I; blue squares), a linear relation between the rate of binding and bulk NeutrAvidin concentration is observed up to a concentration of 5 nM, suggesting mass-transport limited binding kinetics in this regime. For 10 nM, the rate is still higher than for 5 nM, but deviates from the linear trend observed for the lower concentrations. This points toward the onset of reaction-controlled binding kinetics as the number of available binding sites is reduced (NeutrAvidin coverage is increased). The effect becomes even more evident at 100 nM, where the initial rate of binding is 1.2 times smaller than for the 5 nM case. When NeutrAvidin binds on both Au and TiO_2 (case II; red circles), a linear behavior of the concentration dependent binding rate is observed over a significantly wider concentration range. In fact, even at the highest concentration (100 nM), the rate is consistent with the linear trend, which strengthens the interpretation of mass-transport limited binding. Similar binding rates as for case II were observed for case III when NeutrAvidin binds on TiO_2 exclusively, although the rates for primarily case III have, due to small signals and thus sensitivity to drift corrections (−0.0005 $\Delta\lambda/S$ per hour), an uncertainty of around 20%. However, the fact that a clearly detectable signal is recorded at all in case III (as well as upon PLL-*g*-PEG adsorption on TiO_2 [*cf.* inset in Figure 1B]) suggests that the plasmonic field is not strictly confined to the Au region. Although the detailed field distribution cannot be determined from these data alone, the observations are consistent both with theoretical estimates of the field distribution at the substrate/gold interface of plasmonic active holes[37] and measured values of the (average) decay length of the field intensity, which for similar structures were reported to be on the order of 5 to 20 nm.[38,39] The slopes of the linear dependences shown in Figure 2B reveal a 4.3× higher value when proteins bind solely to the Au (case I) compared to binding everywhere on the sensor (case II). Because of the square-root-of-time dependence of the binding rate, this means that it takes 18 times longer in case II to reach the same coverage as in case I, thus demonstrating a significant benefit of directing protein adsorption to the most sensitive Au regions exclusively. Note that, although this was here shown for a nanoplasmonic sensor, the same concept will apply to other optical and also mechanical or electrical nanoscale sensors.

To further evaluate the experimental observations and to aid further improvements of the concept, the differences in binding rates for the three cases were compared with both a rudimentary analytical model and more detailed finite element simulations. The analytical model provides a straightforward insight into the benefit of our approach by displaying the direct relation between the expected binding rate and the reduced bioactive area, thus aiding an intuitive interpretation of the results. The model assumes a flat surface exposed to an infinitely wide and high reservoir of protein solution. To represent mass-transport limited conditions, the concentration just outside the surface is assumed to be much lower than in the bulk solution. The surface is divided into bioactive areas, where proteins can bind, and inert areas, where proteins are repelled. The protein binding rate, here given as the increase in coverage with respect to the saturated surface, can then be expressed as (see SI for a derivation of the expression):

$$\frac{d(c_s/0.55c_{s,max})}{d\sqrt{t}} = \frac{2c_0}{(A_{bind}/A)0.55c_{s,max}}\sqrt{D/\pi} \qquad (2)$$

where $c_{s,max}$ is the maximum attainable protein surface concentration, A_{bind} is the *effective* bioactive surface area, and A is the *projected* total surface area. Note that the effective area of a surface containing nanoholes is larger than its projected area, leading to a lower initial coverage than in the case of a flat surface. In the model, though, the surface is assumed flat and the above effect is taken into account *via* the respective surface ar-

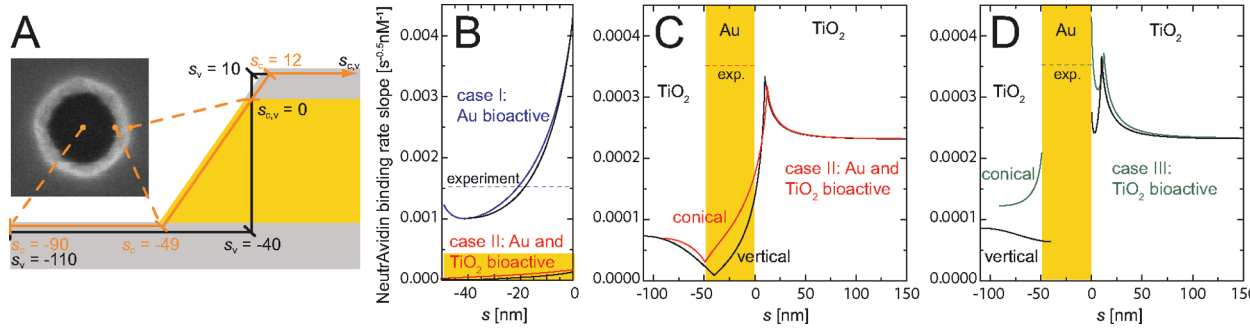

Figure 3. Spatially resolved NeutrAvidin binding rates, determined from finite element (FE) simulations for a 5 nM NeutrAvidin solution 100 s after injection. The values were normalized with the bulk concentration. (A) Schematic side view of the conical hole structure as determined from SEM images (see Materials and Methods for details), with the spatial coordinate s_c (given in nm). FE simulations were also performed for vertical walls (coordinate s_v). The SEM image (200 × 200 nm^2) shows the top-view of a single hole. (B) The binding rate on the Au wall is shown for case I (binding on Au only) and case II (binding on Au and TiO_2). The coordinate s runs from the bottom ($s_c = -49$ nm, $s_v = -40$ nm) to the top ($s_c = s_v = 0$ nm) of the Au film. The binding rate at the top of the Au film is much higher than in the bottom of the hole. Black lines in B−D represent results for the vertical hole geometry. The experimental value is shown as a dashed line. (C) The colored area in panel B is magnified, and the binding rates on the TiO_2 regions are added. It is evident that in case II binding in the hole ($s < 0$ nm) occurs at lower rates than on the top surface ($s_c > 12$ nm, $s_v > 10$ nm). Binding is almost absent in the bottom edge of the hole ($s_c = -49$ nm, $s_v = -40$ nm), while the highest binding rate is observed at the top edge of the hole on TiO_2 ($s_c = 12$ nm, $s_v = 10$ nm). (D) In case III, the rates increase at the interface to the Au region, except for the bottom of the vertical walls ($s_v = -40$ nm).

eas. The factor 0.55 reflects that under random sequential adsorption (RSA) conditions, a maximum of 55% of full coverage can be reached.[40] We compared the cases where molecules can bind to only a fraction of the total surface area ($A_{bind}/A = 0.124$ in case I) and where binding everywhere is allowed ($A_{bind}/A = 1.069$ in case II). The absolute values for the slopes were calculated using $D = 6 \times 10^{-7}$ cm^2/s,[41] and $0.55c_{s,max} = 230$ ng/cm^2 $= 3.83 \times 10^{-8}$ mol/m^2,[42] and normalized with the bulk concentration c_0. The slopes obtained from the analytical model for the cases I and II are then 0.00184 and 0.00021 s$^{-1/2}$ nM^{-1}, respectively. The agreement between the experimental findings and the analytical results is, given the simplistic model, reasonably good, especially for case I. The experimental value is 17% lower than the analytical value for case I, while for case II the experimental value is 67% higher compared to the theoretical values. It is clear from this analysis, as well as from a direct inspection of eq 2, that the relative difference in binding rates between binding everywhere (case II) and the binding on Au only (case I) is a factor of $A_{bind,II}/A_{bind,I}$, i.e. 8.6. The observed difference between case I and case II (factor of 4.3) is a factor of about 2 lower than the analytical model predicts.

Although the analytical model gives a decent theoretical estimate of the binding rates, it does not account for two relevant aspects of the nanoplasmonic sensor: (i) on a surface carrying topographical features such as holes, binding rates must not necessarily be homogeneous over the bioactive sample surface, and (ii) the binding rates alone do not automatically reflect the plasmonic response since an inhomogeneous plasmonic field distribution will make distinct regions of the sensor contribute differently to the total response. The first subject is addressed quantitatively by finite element (FE) simulations of the local binding rates, which also allow a qualitative estimate of the plasmonic field distribution in the holes.

Spatially Resolved NeutrAvidin Binding Rates. Mass-transport limited protein binding to the Au-TiO_2 nanostructured surface was explored by FE simulations using COMSOL Multiphysics 3.5a (COMSOL AB, Stockholm, Sweden). The local binding rates were calculated for a conical hole structure as depicted in Figure 3A, based on the analysis of SEM images (see Materials and Methods for details). The spatial coordinate, s_c, runs along the surface from the center of the bottom of the hole ($s_c = -90$ nm) to its bottom edge ($s_c = -49$ nm), up the Au ($-49 < s_c < 0$ nm) and TiO_2 parts of the wall ($0 < s_c < 12$ nm) and along the top TiO_2 surface ($12 < s_c < 150$ nm). Since the determination of the exact conicity from the SEM images is somewhat uncertain (see Supporting Information), we compared the conical shape with a hole having vertical walls (spatial coordinate s_v, hole radius of 70 nm). Note that the main difference between the two geometries is the TiO_2 bottom surface area, which is about 3 times larger in the case of vertical walls (see Figure 3A), whereas the area of the Au region is approximately the same in the two simulations.

Figure 3 panels B−D show spatially resolved binding rates on the sensor 100 s after protein injection. The situation represents the mass-transport limited case, that is, when the protein surface coverage is well below the saturated coverage. Figure 3B shows significantly higher binding rates for case I (binding on Au only) than for case II (binding everywhere), in accordance to the experimental findings. An interesting result of these simulations is that protein binding occurs in a highly inhomogeneous manner. For case I, binding occurs with a 4 times higher rate at the upper part of the gold region compared with the lower part. This is due to the high association rate constant (k_{on}) for the

NeutrAvidin−biotin interaction,[43] which favors binding of molecules close to the spot where they first interact with the surface. Since an approaching molecule has a higher probability to have its first surface contact at the top part than in the bottom of the hole, the coverage on top will increase faster. However, if k_{on} is assumed to be 1 order of magnitude lower in the simulations (which still represents a biologically relevant regime[44]), the concentration gradient on the Au region is markedly reduced (data not shown). The slight increase of the rate at the lower Au-TiO_2 edge of the hole ($s_c = -49$ nm) is attributed to diffusion of proteins that are repelled from the PEG-modified TiO_2 bottom and instead bind on the biotin-modified Au. A similar behavior in the spatially resolved binding rates is seen in Figure 3C for case II (binding everywhere). The initial binding rate at the bottom of the wall ($s_c = -49$ nm, $s_v = -40$ nm) is markedly lower compared to the top of the wall ($s_c = 12$ nm, $s_v = 10$ nm). Hence, initial binding will occur first at a distance away from the bottom edge, which means that the initial binding might sterically prevent later adsorbing proteins from binding close to the highly sensitive bottom edge region. This, in turn, might have consequences for the final response upon saturation of the surface, as discussed below. In both case I and case II the principal behavior of the binding rates are similar for conical and vertical hole walls. In case III (Figure 3D), the difference between the two hole geometries are more pronounced with a higher binding rate at the bottom of the hole when the walls of the hole are conical. It can also be noted that for the conical case the binding rate increases close to the Au region, whereas for the vertical walls the binding rate changes only little close to the Au parts.

Local Plasmon Field Distribution. The experimental response upon binding on TiO_2 only in case III (see Figure 2A) signals that the field extends a short distance outside the gold region, which is consistent with both previous reports on selective binding to Au−SiO_2-based nanoplasmonic structures[28] as well as with theoretical and experimental estimations of the field distribution around comparable structures.[37] An additional reason to the observed response might be that molecules bind close to the edge in the bottom of the hole and thereby become located very close to the Au film. FE simulations predict that this effect is more pronounced for conical holes (Figure 3D, $s_c = -49$ nm, $s_v = -40$ nm), which might be an indication that the holes are indeed conical, as the inspection of the SEM images suggests. In addition, the flexible nature of the PEG chains[13] and the fact that the biotinylated chains on TiO_2 are slightly longer than the pure PEG chains on Au, means that a slight overlap of the longer chains to the highly sensitive Au region is conceivable. Thus, proteins located at the Au−TiO_2 interface will be sensed and are likely to contribute to the plasmonic response in case III. However, the main contribution is believed to come from the field extending slightly outside the Au region.

TABLE 1. Saturated LSPR Response after Exposing the Substrate to a 100 nM NeutrAvidin Solution for 30 Minutes ($t = 195$ min in Figure 2A). The Standard Deviations Are Retrieved from 2−3 Measurements

	saturated response [$\Delta\lambda/S$]
case I: Au bioactive	0.0046 ± 0.0007
case II: Au and TiO_2 bioactive	0.0046 ± 0.0004
case III: TiO_2 bioactive	0.0020 ± 0.0008

The fractions of the field intensity (which is equal to the square of the field strength) that are located within and outside the gold regions, respectively, are roughly estimated by comparing the saturated response for case I and case III, signaling a 2 times higher response upon binding on Au only (Table 1). This means that two-thirds of the field is located to Au, despite the fact that it occupies around one tenth of the total area. Intuitively one would then expect the total signal upon binding everywhere (case II) to correspond to the sum of the saturated response for case I (binding to Au only) and case III (binding to TiO_2 only). Surprisingly, there is no discernible difference between case I and II, although the sensitivity is expected to extend outside the Au regions (Table 1). A possible explanation is related to the earlier statement that binding in the (highly sensitive) bottom edge of the hole might be sterically prevented in case II. This, in turn, means that the saturated coverage will be effectively lower than in the other cases, hence leading to a lower total plasmonic response upon saturation. Such an argument seems indeed reasonable, since the actual dimensions of the hole (tens of nm) are in the same order as the size of the proteins (~ 5 nm).

This reasoning has one additional important consequence when comparing the simulations with the experimental values under mass-transport limited conditions, that is, at low NeutrAvidin surface coverage. The experimental rate for case II shown in Figures 2B and 3C was normalized with the measured saturated response. However, it should, in order to be accurately compared with the FE simulations, be normalized with a higher saturated response equal to the sum of the saturated response for case I and case III, corresponding to the value that would be obtained if there were no steric hindrance. This is one likely reason for the experimental rate in case II being higher than the FE simulations predict. Another reason might be that the field intensity is expected to be higher by a factor of 4 or even more at the edges than at the middle parts of the Au region for similar structures.[37] Indeed, the application of a localized field intensity to the FE simulations for a conical hole, which is enhanced at the Au−TiO_2 interface and extends 5 to 10 nm into the TiO_2, gives a picture that is consistent with the experimental findings.

However, different factors could influence the results in Figure 3 panels C and D, which make a quantitative comparison of the simulation and the experiments tentative at this stage. First of all, as seen from the simulations of a hole with conical or vertical walls, the actual geometry of the hole can play an important role when estimating the local binding rates, especially for case III (Figure 3D). The concentration profiles over the sensor surface are also sensitive to the value of k_{on} (as stated above). In addition, the 40% higher molecular weight of the SH-PEG-biotin chains compared to the PLL-*g*-PEG-biotin chains may, due to the higher flexibility of the longer chains, affect the association rate constants (k_{on}) for NeutrAvidin binding, thus leading to preferential adsorption on the Au region in the initial stage of adsorption in case II. Furthermore, the PEG chain density on the surface is likely to be higher for shorter chains,[18,34] resulting in different receptor densities on the two surface materials. Also, proteins may not bind according to the RSA model to polymers chains. A saturated coverage exceeding 55% is therefore conceivable because of the ability of long, flexible polymer chains to bind proteins at various distances from the surface.[45] The two last points will, however, not alter the initial binding rates nor the differences obtained between the different surface functionalizations. We cannot at present estimate the relative importance of these effects, but we can emphasize, despite the good agreement between experiments and theoretical estimations, the utmost importance of nanoscale control of the surface chemistries to fully explore the potential of nanoplasmonic as well as other nanoscale sensors.

CONCLUDING REMARKS

We show how material specific surface chemistries of a Au−TiO_2 based nanoplasmonic sensor can be used to direct specific protein binding to the most sensitive regions of the sensor, thereby increasing the response time by a factor of almost 20. This was achieved by material selective surface chemistry, a concept that may be applicable to all types of miniaturized sensors that allows for selective surface modification. This is beneficial in terms of signal-to-noise ratio and an advantage compared to conventional SPR systems, where low concentrations of binding sites must be used to reduce mass-transport effects in kinetic analyses.[46] In our case, a transition to reaction controlled-binding occurs already at around 50% of saturated coverage after exposure to a 5 nM protein solution. With a further reduction of the sensitive area, the challenge of avoiding mass-transport limited binding of slowly diffusing proteins with high association rate constants could be accomplished without flow which typically implies high sample consumption. Micro- or nanofluidic systems[47,48] is an alternative route to approach this challenge and makes a comparison with the present setup relevant. Especially since we recently showed that the sensing performance of LSPR devices of the type used in this work can be preserved on areas as small as 10 × 50 μm^2.[49] In fact, we and others recently showed that nanoplasmonic pores could be used as nanofluidic channels and that such systems could significantly increase the rate of binding for similar reactions.[50,51] An interesting opportunity, that was theoretically investigated by Kim *et al.*,[26] is the combination of microfluidics with the concept presented in this paper. Operating a microfluidic system with a channel size of similar dimensions could increase the response time to a similar extent as observed here. Hence, by combining microfluidics with specific protein binding restricted to the active parts of an LSPR sensor, an additional increase in deposition rate would be obtained until reaction kinetics sets in. However, the actual design of a nanoplasmonic sensor with optimal sensor performance still remains an open question. Both the dimension and the density of the sensitive regions will influence the rate of binding in the mass-transport limited regime as well as the transition from mass-transport limited to reaction-controlled binding. These two parameters also influence the optical properties of the sensor, which will in turn have a direct influence on the signal-to-noise ratio of the system. Hence, the most efficient route toward detection of low abundant analytes will rely on not only selective surface chemistries but also the detailed design of the actual sensor elements, which parts they expose to the analyte-containing solution, and how they are spatially distributed. In this context, the highly inhomogeneous binding rates revealed from FE simulations, demonstrating highest rates occurring at the top edge of the holes, are important. This shows that surfaces bearing topographical features such as holes can be used to create gradients of adsorbates or to concentrate them on a specific spot without applying any external stimuli, especially for systems with high association rate constants. This gives the opportunity to further optimize the sensor topography in order to merge regions of highest binding rates with regions of highest sensitivity. Possibly, this would eventually enable nanoplasmonics to reach single protein sensitivity, which for current state of the art single-particle sensing is still masked by molecules adsorbing in regions of lower sensitivity.[9,49]

MATERIALS AND METHODS

Sample Fabrication. The nanostructured samples were produced by combining colloidal lithography with dry-etching techniques. Circular glass slides (Menzel Gläser) with a diameter of 25 mm and a thickness of 0.2 mm were cleaned in a H_2O:NH_3:H_2O_2 5:1:1 solution at 70 °C for 10 min, then rinsed with H_2O and blow dried with N_2. A 15 nm layer of TiO_2, 40 nm of Au, and again 15 nm TiO_2 were then deposited by sputter coating (FHR MS150). The glass slides were oxygen-plasma cleaned for 2 min (1 kW; Plasma Strip TePla 300PC) before and after the sputtering step. Prior to adsorbing the colloidal particles, the samples were coated with aluminum chlorhydrate (ACH; exposition to a 5 wt % aqueous solution for 1 min, followed by H_2O rinsing for 30 s and N_2 blow drying) to render the surface positively charged. Colloidal

polystyrene particles (diameter 150 nm; Molecular Probes Microspheres Technologies) were adsorbed from a 0.1 wt % aqueous solution for 1 min, rinsed with H_2O for 30 s, submerged by fuming ethylene glycol for 10 s, and further rinsed with H_2O for 30 s before blow drying with N_2. A mild oxygen plasma treatment (2 min, 150 W) increased the particle adhesion and removed the ACH before depositing a 40 nm Au mask by thermal evaporation (Edwards HTPS Auto 306). The colloids were then removed by tape stripping. The sample structure was finalized by (i) reactive ion etching (18 sccm NF_3, 50 sccm Ar; Oxford Plasmalab System 100) for 1 min and (ii) ion beam milling (500 V, 12 mA, 2 sccm Ar; CAIBE Oxford Ionfab) for 2.5 min. Step I etches through the top TiO_2 layer which is not masked by the Au, step II etches away the Au in the holes and removes the Au mask, resulting in a structure as depicted in Figure 1. Note that in step II, about 5 nm of the top TiO_2 layer gets sacrificed in order to ensure complete removal of the Au mask.

Sample Characterization. Samples were characterized by scanning electron microscopy (Zeiss Supra 60 VP), using an acceleration voltage of 15 kV and a high efficiency secondary electron In-lens detector. Images acquired at 50 000× magnification were used to assess the average hole diameter and the hole surface coverage by means of an in house developed MATLAB 2009a (The Mathworks, Natick, MA) program. The holes were detected as connected pixels with an intensity smaller than a user-defined threshold value. The hole number density was determined as 7.2 μm^{-2}. The occurrence of a bright ring in the SEM images (depicting the Au region) suggests a conical shape of the holes. We therefore assessed both the diameters on the bottom and on the top of the holes. For the former, a threshold corresponding to the mean value between the TiO_2 top surface and the bottom of the hole was chosen, giving an average diameter of 83 nm. To determine the diameter at the top of the holes, a threshold corresponding to the mean value between the max intensity from a hole and the flat region was chosen. Assuming that the slope of the hole walls remains the same on TiO_2 as on gold, the average top diameter for a hole was 154 nm. On the basis of these numbers, we determined that 12% of the total surface area is Au. Note that there is a slight discrepancy between what the eye sees as the bright region and the threshold values used in the analysis, resulting in a different perception of the hole conicity (see Supporting Information).

Chemical Surface Modification. Poly(ethylene glycol) (PEG) with thiol anchor groups with or without biotin end groups (SH-PEG, SH-PEG-biotin, respectively) were purchased from Rapp Polymere GmbH, Tübingen, Germany. The molecular weights of the PEGs were 3.3 and 4.8 kDa for SH-PEG and SH-PEG-biotin, respectively. Poly(L-lysine)-*graft*-PEG (PLL-*g*-PEG) and PLL-*g*-PEG-biotin was purchased from Susos AG, Dübendorf, Switzerland. The molecular weights were 20 kDa for the PLL and 2 and 3.4 kDa for the PEG in PLL-*g*-PEG and PLL-*g*-PEG-biotin, respectively. The grafting ratio *g* (*i.e.*, the number of lysine units per grafted PEG chain) was 3.5. NeutrAvidin was purchased from Pierce, USA.

The substrates were first immersed in an aqueous 0.3 mg/mL SH-PEG/SH-PEG-biotin 80:20 solution containing 0.01 M 4-(2-hydroxyethyl)-1-piperazineethanesulfonic acid (HEPES) buffer (pH = 7.4) and 0.9 M Na_2SO_4 for 2 h and then rinsed with H_2O. Second, the samples were exposed to an aqueous 0.01 mg/mL PLL-*g*-PEG solution containing 0.01 M HEPES and 0.15 M NaCl for 1.5 h and then rinsed with H_2O. For samples with only the Au being bioactive (Figure 1C, case I), pure PLL-*g*-PEG was used; for samples with bioactive TiO_2 (Figure 1C, cases II and III), a mixture of PLL-*g*-PEG/PLL-*g*-PEG-biotin 80:20 was used. For experiments with the Au being bioactive only, the samples were chemically modified while already mounted in the titanium flow cell. This allowed for passivation of the cell walls with PLL-*g*-PEG. For the subsequent experiment with biotinylated TiO_2, the chemical surface modification was done prior to mounting the sample in the flow cell. The latter was not cleaned in order to preserve the PLL-*g*-PEG coating. The intactness of the PLL-*g*-PEG layer upon drying and rehydrating has been tested by QCM (E4, Q-Sense AB) with dissipation monitoring. No response was obtained when exposing a TiO_2 crystal (the flow cell surface bears a native TiO_2 layer) to a 170 nM NeutrAvidin solution, showing that the cell walls should not be prone to nonspecific protein adsorption in the experiments of cases II and III (data not shown).

LSPR Setup for Real-Time Monitoring of Surface Processes. The sample was illuminated in transmission mode with white light (wavelength range 500−900 nm) using a tungsten-halogen lamp (HL-2000, Ocean Optics) and a conventional photospectrometer (BRC711E, B&WTek), the components being connected with optical fibers (Ocean Optics). The spectra were recorded with a rate of 0.3 Hz, and the extinction peak position was determined by a centroid approach.[31]

Bulk Sensitivity of the Substrates. The bulk sensitivity of the sensors was assessed after polymer coating by injecting aqueous glycerol solutions of different concentrations (5−30 wt %) and monitoring the peak shift, $\Delta\lambda$, induced by the change in bulk refractive index, ΔRI, of the solution.[52] The so-acquired bulk sensitivity values ($S = \Delta\lambda/\Delta RI$) were used to calibrate the response of the sensor upon NeutrAvidin adsorption. The average bulk sensitivity of the sensors was $S = 98 \pm 13$ nm/refractive index unit (average over eight samples).

NeutrAvidin Adsorption. NeutrAvidin was dissolved in 0.01 M HEPES buffer containing 0.15 M NaCl at different concentrations (1, 2, 5, 10, and 100 nM). Solutions, starting with the lowest concentration, were injected and left under steady conditions in the flow cell for 30 min for NeutrAvidin to adsorb. A buffer rinsing step of 10 min was done prior to the next NeutrAvidin injection. The injection volume (4 mL) was 10× larger than the cell volume to ensure complete liquid exchange.

Finite Element Simulations. The concentration of NeutrAvidin in the solution, *c*, is assumed to be governed by Fick's second law

$$\frac{\partial c(\boldsymbol{x}, t)}{\partial t} = D\frac{\nabla^2 c(\boldsymbol{x}, t)}{\partial \boldsymbol{x}^2} \qquad (3)$$

where $D = 6 \times 10^{-7}$ cm^2/s is the bulk diffusivity of NeutrAvidin in the studied system,[41] *x* is the spatial position, and *t* is the time. The adsorption of molecules to the functionalized surface is, for low coverage, approximated by

$$\frac{\partial c_s(\boldsymbol{s}, t)}{\partial t} = k_{on}c(\boldsymbol{s}, 0, t)(c_{s,max} - 4c_s(\boldsymbol{s}, t)) - k_{off}c_s(\boldsymbol{s}, t) \qquad (4)$$

where $c_s(s,t)$ is the surface coverage at the position **s** on the surface, $c(\mathbf{s},0,t)$ is the bulk concentration immediately outside the surface and $c_{s,max}$ is the surface concentration corresponding to a surface coverage of 100%. To estimate $c_{s,max}$ it is used that the surface concentration saturates at $\sim 3.83 \times 10^{-8}$ mol/m^2,[42] which, assuming that this corresponds to a surface coverage of 55%,[40] yields that $c_{s,max} = 6.96 \times 10^{-8}$ mol/m^2. The two rate constants, k_{on} and k_{off}, have been set to $k_{on} = 2.1 \times 10^8$ M^{-1} s^{-1} and $k_{off} = 3.8 \times 10^{-4}$ s^{-1}.[43]

Equations 3 and 4 were solved using the finite element method with the program COMSOL Multiphysics 3.5a (COMSOL AB) for the three different cases illustrated in Figure 1C. All simulations were made with cylindrical coordinates, and the geometries used are depicted in Figure 3A, where the height of the simulated cell, extending out in the bulk solution, was 1 mm. The width of the unit cell corresponds to a hole coverage of 7.2 holes/μm. The parts of the surface that are functionalized to bind NeutrAvidin were in COMSOL Multiphysics modeled with the following boundary condition

$$\mathbf{n}\cdot D\nabla c = -[k_{on}c(0, s, t)(c_{s,max} - 4c_s(s, t)) - k_{off}c_s(s, t)] \qquad (5)$$

where **n** is a unit normal to the boundary. Equation 5 states that the flux of molecules from the bulk solution toward the surface is equal to the change in surface concentration per time. All other surfaces were set to have the boundary condition $\mathbf{n} \cdot D\nabla c = 0$. The initial conditions for the simulations were $c_s(s,0) = 0$ and $c(x,0) = 5$ nM, and the calculations were stopped at $t = 100$ s. During this time interval the surface coverage increased linearly *versus* $t^{1/2}$ for all three simulated cases. Changing $c(x,0)$ to 1, 2 or 10 nM increased the binding rate proportionally to the bulk concentration but did not change the absorption profile in the simulated time interval.

Acknowledgment. This work was financially supported by the SNSF (Swiss National Science Foundation, Grant No. PBEZA-

121238), the EC FP7 funding (ASMENA) and the SSF (Swedish Foundation for Strategic Research) funded the Ingvar program.

Supporting Information Available: Derivation of the analytical binding rate and characterization of the hole profile. This material is available free of charge *via* the Internet at http://pubs.acs.org.

REFERENCES AND NOTES

1. Ciruela, F. Fluorescence-Based Methods in the Study of Protein−Protein Interactions in Living Cells. *Curr. Opin. Biotechnol.* **2008**, *19*, 338–343.
2. Cooper, M. A.; Singleton, V. T. A Survey of the 2001 to 2005 Quartz Crystal Microbalance Biosensor Literature: Applications of Acoustic Physics to the Analysis of Biomolecular Interactions. *J. Mol. Recognit.* **2007**, *20*, 154–184.
3. Daniels, J. S.; Pourmand, N. Label-Free Impedance Biosensors: Opportunities and Challenges. *Electroanalysis* **2007**, *19*, 1239–1257.
4. Homola, J. Surface Plasmon Resonance Sensors for Detection of Chemical and Biological Species. *Chem. Rev.* **2008**, *108*, 462–493.
5. Burg, T. P.; Godin, M.; Knudsen, S. M.; Shen, W.; Carlson, G.; Foster, J. S.; Babcock, K.; Manalis, S. R. Weighing of Biomolecules, Single Cells and Single Nanoparticles in Fluid. *Nature* **2007**, *446*, 1066–1069.
6. Shekhawat, G.; Tark, S. H.; Dravid, V. P. MOSFET-Embedded Microcantilevers for Measuring Deflection in Biomolecular Sensors. *Science* **2006**, *311*, 1592–1595.
7. Stern, E.; Klemic, J. F.; Routenberg, D. A.; Wyrembak, P. N.; Turner-Evans, D. B.; Hamilton, A. D.; LaVan, D. A.; Fahmy, T. M.; Reed, M. A. Label-Free Immunodetection with CMOS-Compatible Semiconducting Nanowires. *Nature* **2007**, *445*, 519–522.
8. Anker, J. N.; Hall, W. P.; Lyandres, O.; Shah, N. C.; Zhao, J.; Van Duyne, R. P. Biosensing with Plasmonic Nanosensors. *Nat. Mater.* **2008**, *7*, 442–453.
9. Nusz, G. J.; Curry, A. C.; Marinakos, S. M.; Wax, A.; Chilkoti, A. Rational Selection of Gold Nanorod Geometry for Label-Free Plasmonic Biosensors. *ACS Nano* **2009**, *3*, 795–806.
10. Anderson, N. L.; Anderson, N. G. The Human Plasma Proteome−History, Character, and Diagnostic Prospects. *Mol. Cell. Proteomics* **2002**, *1*, 845–867.
11. Rifai, N.; Gillette, M. A.; Carr, S. A. Protein Biomarker Discovery and Validation: The Long and Uncertain Path to Clinical Utility. *Nat. Biotechnol.* **2006**, *24*, 971–983.
12. Bell, J. Predicting Disease Using Genomics. *Nature* **2004**, *429*, 453–456.
13. Harris, J. M. *Poly(ethylene glycol) Chemistry, Biotechnical and Biomedical Applications*; Plenum Press: New York and London, 1992.
14. Unsworth, L. D.; Sheardown, H.; Brash, J. L. Protein Resistance of Surfaces Prepared by Sorption of End-Thiolated Poly(ethylene glycol) to Gold: Effect of Surface Chain Density. *Langmuir* **2005**, *21*, 1036–1041.
15. Jo, S.; Park, K. Surface Modification Using Silanated Poly(ethylene glycol)s. *Biomaterials* **2000**, *21*, 605–616.
16. Zurcher, S.; Wackerlin, D.; Bethuel, Y.; Malisova, B.; Textor, M.; Tosatti, S.; Gademann, K. Biomimetic Surface Modifications Based on the Cyanobacterial Iron Chelator Anachelin. *J. Am. Chem. Soc.* **2006**, *128*, 1064–1065.
17. Dalsin, J. L.; Lin, L. J.; Tosatti, S.; Voros, J.; Textor, M.; Messersmith, P. B. Protein Resistance of Titanium Oxide Surfaces Modified by Biologically Inspired mPEG-DOPA. *Langmuir* **2005**, *21*, 640–646.
18. Pasche, S.; De Paul, S. M.; Voros, J.; Spencer, N. D.; Textor, M. Poly(L-lysine)-graft-poly(ethylene glycol) Assembled Monolayers on Niobium Oxide Surfaces: A Quantitative Study of the Influence of Polymer Interfacial Architecture on Resistance to Protein Adsorption by ToF-SIMS and *in Situ* OWLS. *Langmuir* **2003**, *19*, 9216–9225.
19. Amiji, M.; Park, K. Prevention of Protein Adsorption and Platelet-Adhesion on Surfaces by PEO/PPO/PEO Triblock Copolymers. *Biomaterials* **1992**, *13*, 682–692.
20. Huang, N. P.; Voros, J.; De Paul, S. M.; Textor, M.; Spencer, N. D. Biotin-Derivatized Poly(L-lysine)-*g*-poly(ethylene glycol): A Novel Polymeric Interface for Bioaffinity Sensing. *Langmuir* **2002**, *18*, 220–230.
21. Todd, S. J.; Scurr, D. J.; Gough, J. E.; Alexander, M. R.; Ulijn, R. V. Enzyme-Activated RGD Ligands on Functionalized Poly(ethylene glycol) Monolayers: Surface Analysis and Cellular Response. *Langmuir* **2009**, *25*, 7533–7539.
22. Heyes, C. D.; Groll, J.; Moller, M.; Nienhaus, G. U. Synthesis, Patterning, and Applications of Star-Shaped Poly(ethylene glycol) Biofunctionalized Surfaces. *Mol. Biosyst.* **2007**, *3*, 419–430.
23. Michel, R.; Lussi, J. W.; Csucs, G.; Reviakine, I.; Danuser, G.; Ketterer, B.; Hubbell, J. A.; Textor, M.; Spencer, N. D. Selective Molecular Assembly Patterning: A New Approach to Micro- and Nanochemical Patterning of Surfaces for Biological Applications. *Langmuir* **2002**, *18*, 3281–3287.
24. Falconnet, D.; Koenig, A.; Assi, T.; Textor, M. A Combined Photolithographic and Molecular-Assembly Approach to Produce Functional Micropatterns for Applications in the Biosciences. *Adv. Funct. Mater.* **2004**, *14*, 749–756.
25. Larsson, A.; Du, C. X.; Liedberg, B. UV-Patterned Poly(ethylene glycol) Matrix for Microarray Applications. *Biomacromolecules* **2007**, *8*, 3511–3518.
26. Kim, D. R.; Zheng, X. L. Numerical Characterization and Optimization of the Microfluidics for Nanowire Biosensors. *Nano Lett.* **2008**, *8*, 3233–3237.
27. Dahlin, A. B.; Jonsson, M. P.; Hook, F. Specific Self-Assembly of Single Lipid Vesicles in Nanoplasmonic Apertures in Gold. *Adv. Mater.* **2008**, *20*, 1436–1442.
28. Marie, R.; Dahlin, A. B.; Tegenfeldt, J. O.; Hook, F. Generic Surface Modification Strategy for Sensing Applications Based on Au/SiO_2 Nanostructures. *Biointerphases* **2007**, *2*, 49–55.
29. Tosatti, S.; De Paul, S. M.; Askendal, A.; VandeVondele, S.; Hubbell, J. A.; Tengvall, P.; Textor, M. Peptide Functionalized Poly(L-lysine)-*g*-poly(ethylene glycol) on Titanium: Resistance to Protein Adsorption in Full Heparinized Human Blood Plasma. *Biomaterials* **2003**, *24*, 4949–4958.
30. Hanarp, P.; Sutherland, D. S.; Gold, J.; Kasemo, B. Control of Nanoparticle Film Structure for Colloidal Lithography. *Colloids Surf., A* **2003**, *214*, 23–36.
31. Dahlin, A. B.; Tegenfeldt, J. O.; Hook, F. Improving the Instrumental Resolution of Sensors Based on Localized Surface Plasmon Resonance. *Anal. Chem.* **2006**, *78*, 4416–4423.
32. Jonsson, M. P.; Dahlin, A. B.; Jonsson, P.; Hook, F. Nanoplasmonic Biosensing with Focus on Short-Range Ordered Nanoholes in Thin Metal Films. *Biointerphases* **2008**, *3*, FD30–FD40.
33. Laibinis, P. E.; Hickman, J. J.; Wrighton, M. S.; Whitesides, G. M. Orthogonal Self-Assembled Monolayers—Alkanethiols on Gold and Alkane Carboxylic-Acids on Alumina. *Science* **1989**, *245*, 845–847.
34. Feuz, L.; Leermakers, F. A. M.; Textor, M.; Borisov, O. Adsorption of Molecular Brushes with Polyelectrolyte Backbones onto Oppositely Charged Surfaces: A Self-Consistent Field Theory. *Langmuir* **2008**, *24*, 7232–7244.
35. Skvortsov, A. M.; Gorbunov, A. A.; Leermakers, F. A. M.; Fleer, G. J. Long Minority Chains in a Polymer Brush: A First-Order Adsorption Transition. *Macromolecules* **1999**, *32*, 2004–2015.
36. Cussler, E. L. *Diffusion: Mass Transfer in Fluid Systems*; Cambridge University Press: Cambridge, U.K., 1997.
37. Rindzevicius, T.; Alaverdyan, Y.; Sepulveda, B.; Pakizeh, T.; Kall, M.; Hillenbrand, R.; Aizpurua, J.; de Abajo, F. J. G. Nanohole Plasmons in Optically Thin Gold Films. *J. Phys. Chem. C* **2007**, *111*, 1207–1212.
38. Rindzevicius, T.; Alaverdyan, Y.; Dahlin, A.; Hook, F.; Sutherland, D. S.; Kall, M. Plasmonic Sensing Characteristics of Single Nanometric Holes. *Nano Lett.* **2005**, *5*, 2335–2339.
39. Jonsson, M. P.; Jonsson, P.; Hook, F. Simultaneous Nanoplasmonic and Quartz Crystal Microbalance Sensing:

Analysis of Biomolecular Conformational Changes and Quantification of the Bound Molecular Mass. *Anal. Chem.* **2008**, *80*, 7988–7995.
40. Luthgens, E.; Janshoff, A. Equilibrium Coverage Fluctuations: A New Approach to Quantify Reversible Adsorption of Proteins. *ChemPhysChem* **2005**, *6*, 444–448.
41. Spinke, J.; Liley, M.; Schmitt, F. J.; Guder, H. J.; Angermaier, L.; Knoll, W. Molecular Recognition at Self-Assembled Monolayers: Optimization of Surface Functionalization. *J. Chem. Phys.* **1993**, *99*, 7012–7019.
42. Jung, L. S.; Nelson, K. E.; Stayton, P. S.; Campbell, C. T. Binding and Dissociation Kinetics of Wild-Type and Mutant Streptavidins on Mixed Biotin-Containing Alkylthiolate Monolayers. *Langmuir* **2000**, *16*, 9421–9432.
43. Wayment, J. R.; Harris, J. M. Biotin−Avidin Binding Kinetics Measured by Single-Molecule Imaging. *Anal. Chem.* **2008**, *81*, 336–342.
44. Bongrand, P. Ligand−Receptor Interactions. *Rep. Prog. Phys.* **1999**, *62*, 921–968.
45. Longo, G.; Szleifer, I. Ligand−Receptor Interactions in Tethered Polymer Layers. *Langmuir* **2005**, *21*, 11342–11351.
46. Goldstein, B.; Coombs, D.; He, X. Y.; Pineda, A. R.; Wofsy, C. The Influence of Transport on the Kinetics of Binding to Surface Receptors: Application to Cells and Biacore. *J. Mol. Recognit.* **1999**, *12*, 293–299.
47. Whitesides, G. M. The Origins and the Future of Microfluidics. *Nature* **2006**, *442*, 368–373.
48. Eijkel, J. C. T.; van den Berg, A. Nanofluidics: What Is It and What Can We Expect from It. *Microfluid. Nanofluid.* **2005**, *1*, 249–267.
49. Dahlin, A. B.; Chen, S.; Jonsson, M. P.; Gunnarsson, L.; Kall, M.; Hook, F. High-Resolution Microspectroscopy of Plasmonic Nanostructures for Miniaturized Biosensing. *Anal. Chem.* **2009**, *81*, 6572–6580.
50. Jonsson, M. P.; Dahlin, A.; Feuz, L.; Petronis, S.; Hook, F. Locally Functionalized Short-Range Ordered Nanoplasmonic Pores for Bioanalytical Sensing. *Anal. Chem.* **2010**, *82*, 2087–2094.
51. Eftekhari, F.; Escobedo, C.; Ferreira, J.; Duan, X. B.; Girotto, E. M.; Brolo, A. G.; Gordon, R.; Sinton, D. Nanoholes as Nanochannels: Flow-through Plasmonic Sensing. *Anal. Chem.* **2009**, *81*, 4308–4311.
52. Hoyt, L. New Table of the Refractive Index of Pure Glycerol at 20°C. *Ind. Eng. Chem.* **1934**, *26*, 329–332.